Available online at www.sciencedirect.com
ScienceDirect
ELSEVIER
Ultramicroscopy 108 (2008) 791–803
ultramicroscopy
www.elsevier.com/locate/ultramic

Effects of amorphous layers on ADF-STEM imaging

K.A. Mkhoyan*, S.E. Maccagnano-Zacher, E.J. Kirkland, J. Silcox

School of Applied and Engineering Physics, Cornell University, Ithaca, NY 14853, USA

Received 15 June 2007; received in revised form 17 November 2007; accepted 23 January 2008

Abstract

A study of high-resolution ADF imaging in uncorrected and aberration-corrected STEMs was carried out by multislice simulation. The presence of amorphous layers at the surface of a crystalline specimen is shown to significantly alter the visibility of the atomic columns. After propagating through an amorphous layer a portion of the beam passes without any alteration while scattered electrons introduce a Gaussian background. The dependence of the image contrast on the crystal structure, orientation and the types of the atoms present in the crystal was studied. In the case of uncorrected probes an amorphous layer thicker than 200 Å is necessary to achieve considerable reduction of the visibility of the atomic columns, but with aberration-corrected probes only 60 Å is necessary. With changes in defocus, crystalline specimens with amorphous layers on the top can also be imaged and high-resolution ADF images can be obtained. An amorphous layer at the beam entry surface affects the ADF image more than that of an amorphous layer at the exit surface. Approximately linear reduction of the contrast (with a slop of 1) is expected with increased thickness of amorphous layer.
© 2008 Elsevier B.V. All rights reserved.

PACS: 68.37.Ma; 61.43.Bn; 61.05.J–

Keywords: STEM; ADF imaging; Aberration correction; Multislice simulation; Si

1. Introduction

Very often layers of amorphous material are present on the surfaces of crystalline specimens prepared for study in conventional transmission electron microscopes (TEMs) or scanning-TEMs (STEMs). The reasons for the presence of the amorphous layers in these specimens vary. Preparation of thin, electron-transparent specimens is often carried out by manual polishing [1–3] or ion milling [4,5]. Both methods almost always result in the creation of amorphous layers on the polished/milled surfaces, although the thickness of these layers varies with technique, setup and operator skills. Amorphous carbon films often serve as supports for specimens such as quantum dots, rods and wires. In some cases specimens are sensitive to electron-beam-induced knock-on damage [6,7]. For these samples the surfaces are often intentionally covered with a layer of amorphous carbon for protection [7].

The presence of an amorphous layer on the surfaces of crystalline specimens is expected to have an effect on high-resolution annular dark field (ADF) imaging, most likely producing a reduction in contrast. However, it is not clear what the limits are and how exactly the presence of the amorphous layers will effect imaging in the ADF-STEM. It is also not clear what the differences in contrast will be when specimens are imaged with uncorrected probes or aberration-corrected sub-Å probes [8–10]. Some studies of the effects of an amorphous layer on the probe modification and ADF-STEM imaging have been reported previously [11,12], wherein primarily uncorrected probes were considered.

In this paper we present an extensive study of the possible effects that amorphous layers may have on high-resolution ADF-STEM image formation and on the visibility of atomic columns. This study was carried out using a computational multislice method. The multislice method [13] has been successfully implemented to understand experimental observations of the relative contrast levels of crystal lattice fringes as a function of defocus

*Corresponding author. Tel.: +1 607 255 0649.
E-mail address: kam55@cornell.edu (K.A. Mkhoyan).

0304-3991/$ - see front matter © 2008 Elsevier B.V. All rights reserved.
doi:10.1016/j.ultramic.2008.01.007

[14–17], specimen thickness [17], and convergence-beam electron diffraction (CBED) patterns [18,19]. A correlation between measured beam broadening during characterization of the GaN/AlN quantum wells and predictions by multislice methods has also been shown [20].

2. Multislice ADF-STEM simulations

The algorithm for calculation of the ADF-STEM images is based on the multislice method [13]. First, a STEM focused electron probe is generated using the experimental parameters. The wave function of the STEM probe located at point $\vec{x}_p$ is defined as

$$\psi_p(\vec{x}) = A_p \int_0^{k_{\max}} \exp[-i\chi(\vec{k}) - 2\pi i\vec{k}(\vec{x} - \vec{x}_p)]\, d^2\vec{k}, \tag{1}$$

where $\lambda k_{\max} = \alpha_{\max}$ the maximum angle allowed by the objective aperture, $\chi(\vec{k})$ is the aberration function and A_p is a normalization constant. Then the incident electron beam is propagated through the entire thickness of the specimen by alternately passing through thin layers of the specimen and propagating between the layers. The ADF intensity is calculated by summing up all of the electrons that are elastically scattered from the atoms of the specimen into the conical solid angle of the ADF detector. The final image is generated by scanning the probe position across a small area of the model specimen [21].

The crystalline Si (c-Si) specimen model for the simulations was constructed by locating the electrostatic atomic potentials of Si atoms in the corresponding lattice sites of the diamond crystal structure with Si lattice constant of $a = 5.42$ Å.

Thermal vibrations of the atoms (or phonons) are included in the calculation by randomly displacing atoms from their lattice sites using a Gaussian distribution with the corresponding Debye–Waller factors [14]. The amorphous layers were constructed using c-Si as a starting point and displacing atoms so far that layers lose all possible periodicities (as a result the amorphous layers have the same density as the crystals). More realistic models for amorphous Si exist in the literature, but this model is a sufficiently good approximation for this study of electron beam scattering.

The ADF-STEM simulations presented in this paper were performed primarily on Si specimens. The sizes of the Si supercells used in the calculations were: 27.15×26.88 Å^2 for the sample oriented along the [1 1 0] direction and 27.15×27.15 Å^2 and 26.88×26.60 Å^2 for the samples along [1 0 0] and [1 1 1], respectively. The images were obtained by scanning the probe over a 12×12 Å^2 area in the middle of the supercell with 70×70 steps. The following slice thicknesses were used in all simulations: 1.920 Å in the crystals aligned along [1 1 0] and 3.135 and 1.357 Å for the crystals along [1 0 0] and [1 1 1], respectively. The inner and outer angles of the ADF detector were 54 and 340 mrads. All calculated ADF intensities are normalized with respect to the incident beam and, because the incident probe intensities in all calculations are kept the same, they are all normalized to the same value. This normalization to a single incident electron is essential for a quantitative comparison of different ADF intensities.

Two STEM probes have been considered for this study. A $\simeq 2$ Å probe was generated by using the following electron optical parameters: 100 kV acceleration voltage, spherical aberration of $C_s = 1.3$ mm, objective angle of 11.4 mrad, and defocus of 850 Å. While these numbers are typical for the Cornell VG-HB501 STEM, they are also comparable to the optical conditions of other STEMs with similar resolutions. A new probe of $\simeq 0.8$ Å was created using corrections to the axial aberrations: acceleration

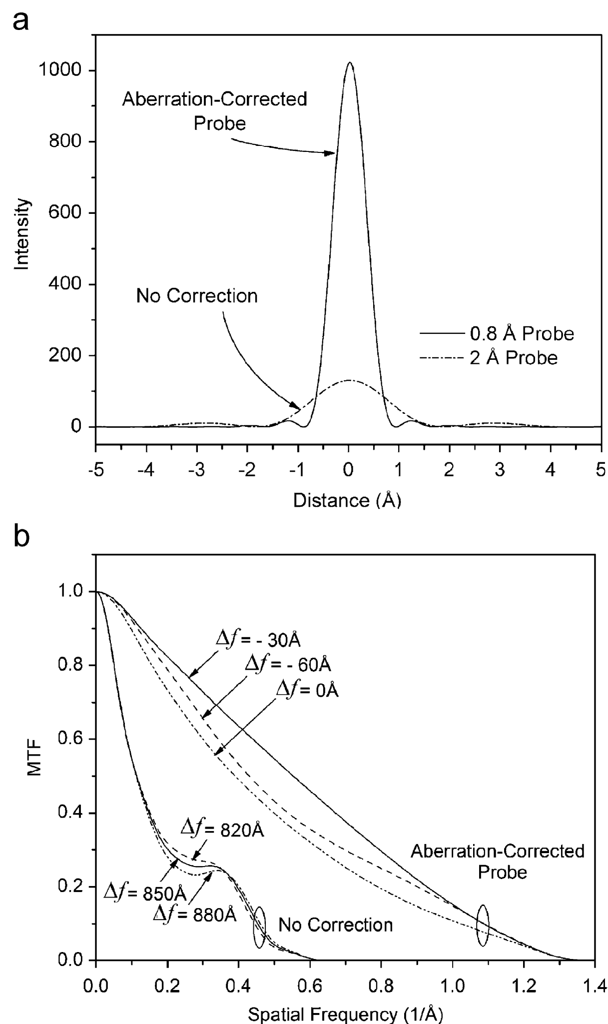

Fig. 1. (a) Line profiles of two STEM probes: uncorrected 2 Å probe and aberration-corrected 0.8 Å probe. These two probes are normalized to the same total intensity. The optical parameters used in the calculations are: for non-corrected probe: $E_0 = 100$ kV, $C_s = 1.3$ mm, $\alpha_{obj} = 11.4$ mrad, and $\Delta f = 850$ Å, and for aberration-corrected probe: $E_0 = 100$ kV, $C_{s(3)} = -0.015$ mm, $C_5 = 10$ mm, $\alpha_{obj} = 25$ mrad, and $\Delta f = -30$ Å. (b) ADF-STEM transfer functions for the two probes in (a) with changes in defocus of ± 30 Å.

voltage of 100 kV, $C_{s(3)} = -0.015$ mm, $C_5 = 10$ mm, objective angle of 25 mrad, and defocus of −30 Å close to the conditions used in Ref. [10]. Chromatic aberration is not included in these probe calculations. The profiles of these two probes and corresponding ADF transfer functions are presented in Fig. 1. Both probes have the same total intensities. The visibility of the atomic columns in pure c-Si was also studied experimentally and with multislice simulation by Batson for 120 kV STEM [22].

3. Results

Before discussing the effects of the amorphous layers on the surfaces of the crystalline specimens it is critical to address the issue of what is the optimal focusing condition for the STEM probe relative to specimen. To clarify this several ADF-STEM image linescans across Si dumbbells (in [1 1 0] projection) were calculated using an aberration-corrected 0.8 Å probe by focusing the probe at different

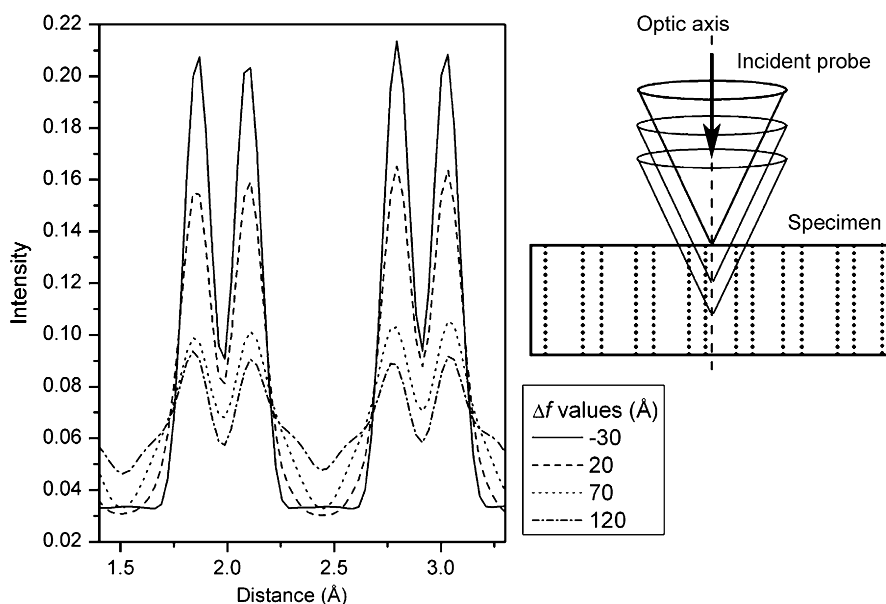

Fig. 2. Series of linescans along the dumbbells of Si crystal showing the visibility of the atomic columns in ADF-STEM images. ADF intensities are calculated for 300 Å thick specimen with a 0.8 Å probe. Probes focused at different depth from the top (entry) surface are considered here. The schematic diagram is presented on the right.

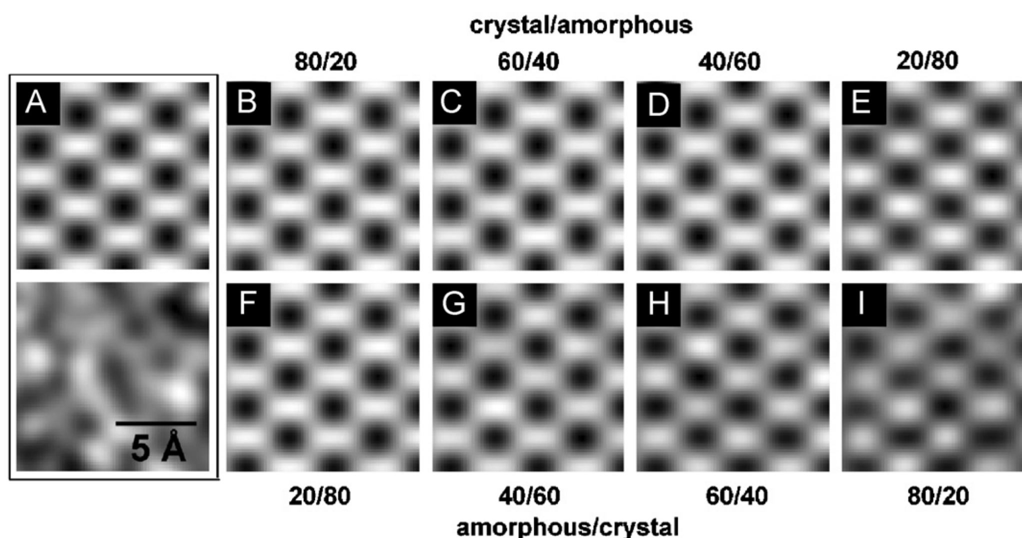

Fig. 3. Simulated ADF-STEM images of 300 Å silicon specimens consisting of crystalline and amorphous layers. The 2 Å probe was oriented along the [1 1 0] crystallographic direction. Images in (A) are pure crystalline (top) and amorphous (bottom) silicon. Images (B–E) were calculated for 80% crystal and 20% amorphous, then 60% and 40%, 40% and 60%, 20% and 80% specimens. Here the probe propagates through the crystal part first and then through the amorphous layer. Images (F–I) are calculated similarly to the previous images but the probe enters the amorphous layer first and then the crystalline layer. All images are individually scaled to fill the available grayscale.

depths in the specimen. The results are presented in Fig. 2. The depth of focus for this probe is estimated to be ≈ 40 Å and, therefore, 50 Å steps were chosen in these calculations. As Fig. 2 shows, the best contrast in ADF images of crystals occurs when the probe is focused on the entrance surface of the specimen. Therefore, in the proceeding section we discuss the contrast in high-resolution ADF images by focusing the beam mostly on the entrance surface of the specimen. It should be noted that slight fluctuations in the intensity values from similar points in these linescans are due to finite sampling of the images during simulation.

3.1. Uncorrected probe

ADF-STEM images of silicon specimens calculated using the 2 Å probe are presented in Fig. 3. Two cases were considered here: (i) the exit surface of the specimen is covered with an amorphous layer and (ii) the entrance surface contains an amorphous layer. While the total thickness of the specimen was kept at 300 Å, the proportions of crystal to amorphous layers were varied from 100% crystal to 100% amorphous. Every image in Fig. 3 is individually scaled to fill the available grayscale as in most displayed experimental images. This often enhances the visibility of small features or small contrast in the image.

As expected, even for pure crystalline specimens the individual atomic columns in the dumbbells are not resolved due to insufficient spatial resolution. However, the pairs are quite distinct and their visibility is essentially unaffected by the presence of the amorphous layers. These simulations suggest that when the probe propagates through the crystalline part first, 20% of the crystal is sufficient to identify the dumbbell units clearly relative to the background (see Fig. 3 panel (E)). In the case where the probe propagates through the amorphous layer first, the reduction in visibility of the crystal structure becomes apparent when the sample is reduced to 20% crystal (see Fig. 3 panel (I)). For quantitative analysis of the visibility of atomic columns in the images, the contrast ξ was calculated using a simple formula:

$$\xi = \frac{I_{\max} - I_{\min}}{I_{\text{mean}}}, \tag{2}$$

where $I_{\max}$ is the intensity at the position of the atomic column, $I_{\min}$ is the intensity between the dumbbells and I_{mean} is the mean intensity of the entire ADF image. This definition of the contrast allows comparison with experimental contrast data which can be deduced from Fourier analysis of the images (the zero spot in the power spectrum of an image corresponds to its mean value). It should be noted that contrast defined in Eq. (2) describes the visibility of the atomic columns and should not be confused with a more general definition of contrast applicable to any given image. The contrast values corresponding to the results in Fig. 3 and calculated for different proportions of crystal and amorphous layers are presented in Fig. 4. For noise reduction in the data, the values of $I_{\max}$ and $I_{\min}$ were averaged over many identical locations on the image. It should be noted that since the contrast of the atomic columns in amorphous material cannot be defined, we used the definition of the contrast for crystalline specimens (2) and extended it to amorphous material; i.e., the intensities of the same points in the images used to calculate the contrast in the crystal are also used to calculate contrast in amorphous (or partially amorphous) material.

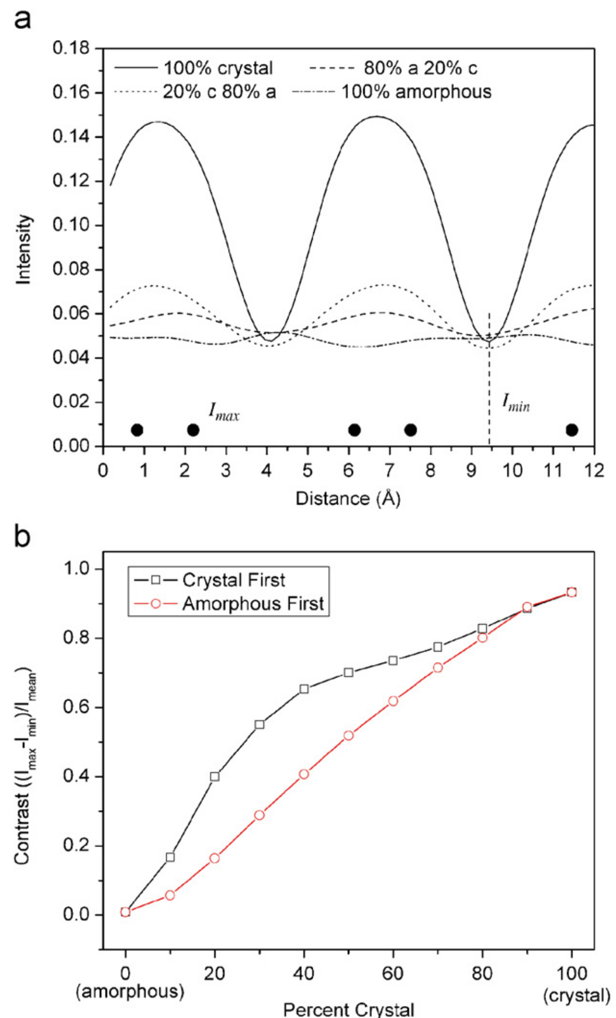

Fig. 4. Visibility of the atomic columns in ADF-STEM images calculated for 300 Å thick silicon specimens with a 2 Å probe. The crystalline portion is along the [1 1 0] direction. (a) Series of linescans taken from the images presented in panels (A), (E), (I) and (J) of Fig. 3 along the dumbbells. (b) Calculated contrast as a function of the percentage of amorphous layers for two cases: the beam propagates through the crystal first and the beam propagates through amorphous layers first. The positions of the points whose intensities were used in the calculation of the contrast are indicated in (a).

According to the simulations, for STEM with a 2 Å probe the crystal structure should be visible in ADF images even when 90% of the specimen is amorphous (see Fig. 4(b)). The second critical observation is that the visibility of the dumbbells is higher when the beam propagates through the crystal first.

3.2. Aberration-corrected probe

Simulations were also carried out for a STEM with an aberration-corrected 0.8 Å probe. While a new probe was generated for these calculations, all the remaining parameters were kept the same as those in the simulations presented in Fig. 3. The resulting ADF images are presented in Fig. 5. As expected, for a pure crystalline specimen the 0.8 Å STEM probe clearly resolves individual atomic columns of the dumbbell (1.36 Å separation). However, unlike the 2 Å probe, simulations with the 0.8 Å probe show significantly lower visibility of the atomic columns when the beam propagates through the amorphous layer first. Further analysis shows that if the STEM probe is focused not at the sample entry surface but defocused to a depth inside the specimen where the crystalline portion starts, high-resolution ADF images can still be obtained. Fig. 5(J–M) shows high-resolution ADF images of the specimen with the amorphous layer at the entry surface when the beam is focused at the surface of the crystalline portion.

Quantitative analysis of the contrast for this case is presented in Fig. 6. It shows that when the beam propagates through the crystal first the atomic columns are clearly resolved even for specimens with only 10% crystal. However, when the 0.8 Å probe propagates through the amorphous layer first, the contrast is practically zero until the crystalline layer is thicker than 60% of the total thickness. This suggests that stronger beam spreading in the amorphous layer takes place when the probe is aberration-corrected. The visibility of the atomic columns in ADF-STEM images using an aberration-corrected probe is expected to have significant gain compared to the conventional 2 Å probe: for 60% crystalline specimens $\xi_{0.8} \simeq 2.0$ and $\xi_2 \simeq 0.7$. ADF-STEM images calculated using the 0.8 Å probe show that a significant reduction or complete loss of visibility of the atomic columns becomes an issue for concern only in cases where the probe, focused at the specimen surface, propagates through the amorphous layer first.

In Figs. 4(b) and 6(b), contrast was calculated using I_{min} as the intensity between the dumbbells, In Fig. 6(c), however, I_{min} is redefined as the intensity between the individual columns in the dumbbell itself. This shows that the contrast curves representing the visibility of the columns in the dumbbell closely follow the trend of the general contrast.

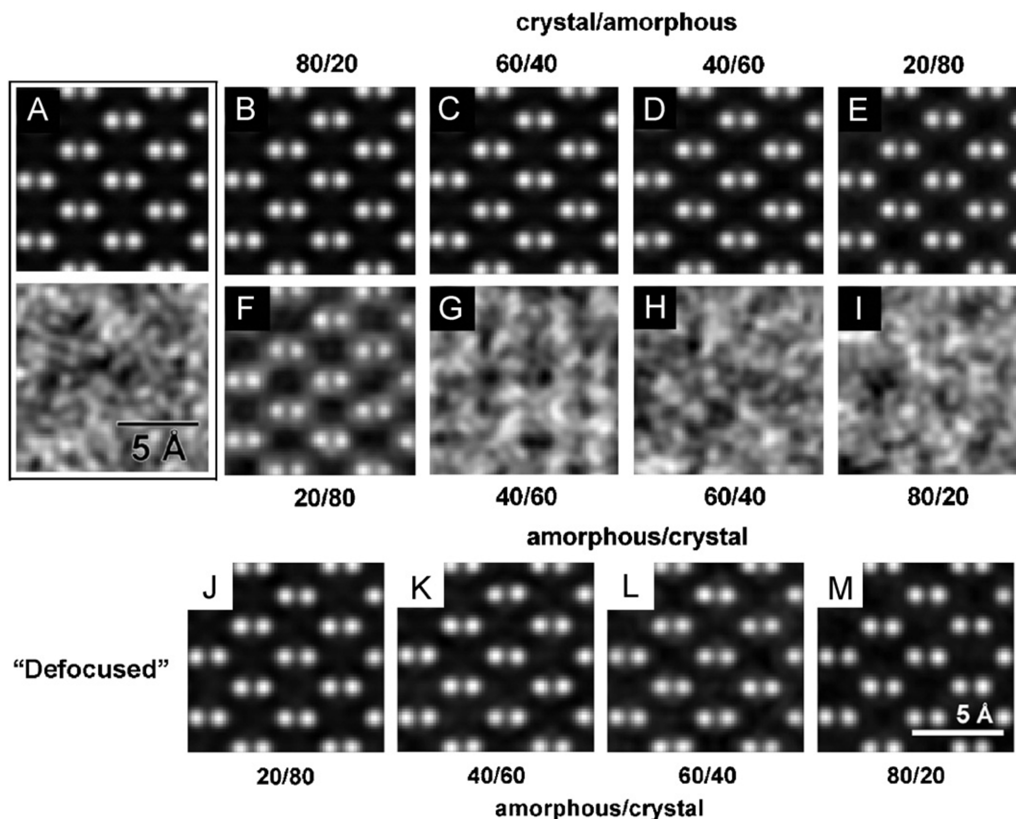

Fig. 5. Simulated ADF-STEM images of 300 Å silicon specimens consisting of crystalline and amorphous layers. The 0.8 Å probe was used and crystal layers were oriented along the [1 1 0] crystallographic direction. Images in (A) are pure crystalline (top) and amorphous (bottom) silicon. Images (B–E) were calculated for 80% crystal and 20% amorphous, then 60% and 40%, 40% and 60%, 20% and 80% specimens. Here the probe propagates through the crystal first and then through the amorphous material. Images (F–I) are calculated as in the previous images but the probe enters the amorphous layer first and then the crystalline layers. Images (J–M) are from the same samples as (F–I) correspondingly but now the beam is focused (or "defocused" from surface) at the entrance surface of the crystalline portion. All images are individually scaled to fill available grayscale.

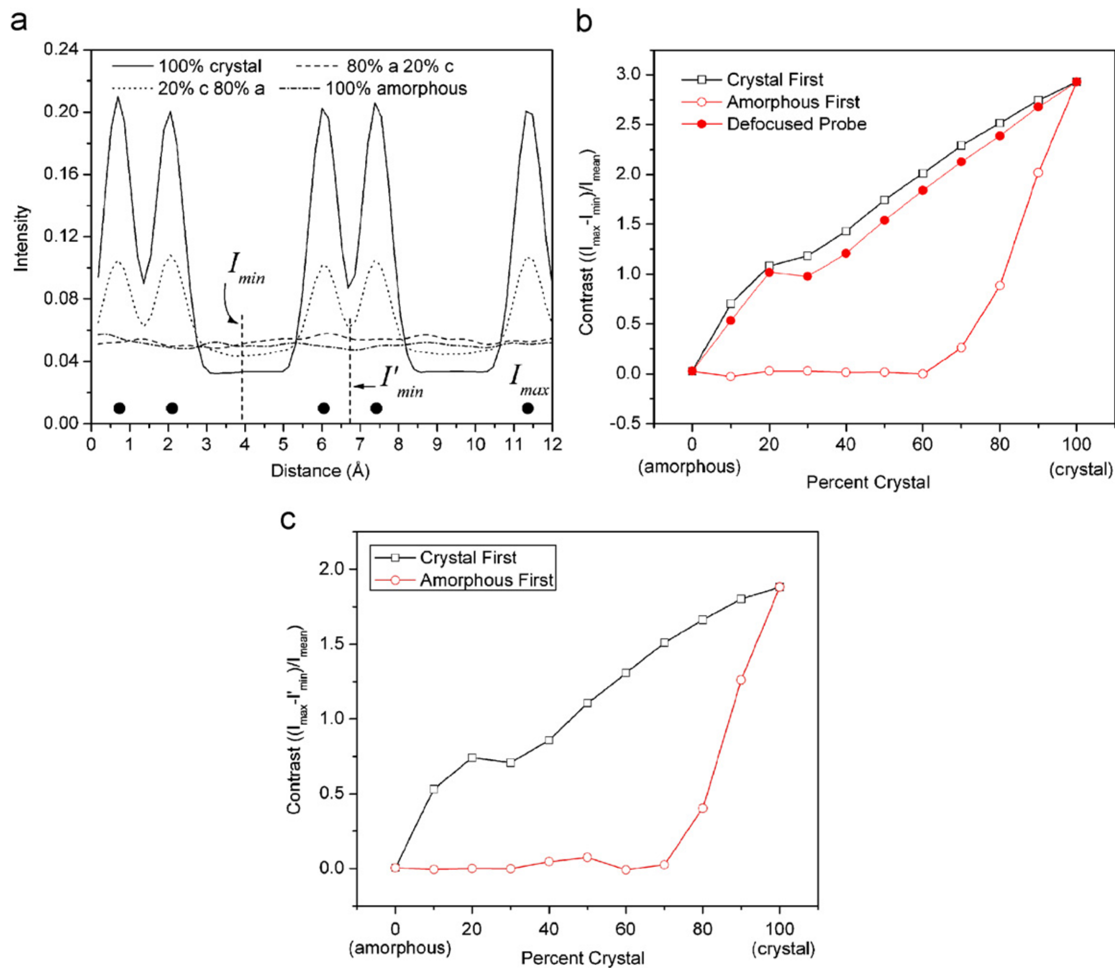

Fig. 6. Visibility of the atomic columns in ADF-STEM images calculated for 300 Å thick silicon specimens with a 0.8 Å probe. The crystalline portion is oriented along the [1 1 0] direction. (a) Series of linescans along the dumbbells taken from the images presented in panels (A), (E), (I) and (J) of Fig. 5. (b). Calculated contrast as a function of percentage of amorphous layers for two cases: the beam propagates through the crystal first and through the amorphous layer first. The values of contrast when the beam is focused (or "defocused" from surface) at the entrance surface of the crystalline portion are also presented. (c) Contrast of atomic columns in dumbbells calculated using I'_{min} instead of I_{min} in Eq. (2). The positions of the points whose intensities were used in the calculation are indicated in (a).

3.2.1. Different crystallographic orientations

Since the electron beam is expected to channel along atomic columns differently for different crystallographic directions, a new set of ADF-STEM images were calculated for the same silicon specimen in new orientations. Here specimens with 50% amorphous and 50% crystalline layers were considered. The new Si specimens were modeled with the crystalline part oriented along the [1 0 0] or [1 1 1] direction. As before, the total thickness of the specimen was kept at 300 Å. The results of these simulations are presented in Fig. 7. It appears that for all three major orientations in Si the general results are the same: (i) the atomic columns are invisible when the beam, focused at the specimen surface, propagates through the amorphous layer first and, (ii) when probe is focused on the crystal entrance surface, the columns are clearly identifiable. The actual numbers for the contrast indicate that for the latter case the visibility of columns grows depending on orientation, from [1 0 0] to [1 1 1] to [1 1 0]. Over a 100% increase in contrast is observed going from a [1 0 0] direction to a [1 1 0]. Note that the structures of the amorphous Si layers are independent of orientation. As can be seen from Fig. 7(a) with the amorphous layer at the entry surface when beam is focused at the depth where crystalline portion starts the contrast in high-resolution ADF images follows the trend of the crystal first sample.

3.2.2. Different atomic species

Hillyard and Silcox [23] showed that when the electron beam propagates through two crystals with the same crystal structure and lattice constants but different atom species, the beam may channel considerably differently. To study the effects of the atomic number on the visibility of the columns in the presence of an amorphous layer, we calculated ADF images of hypothetical crystals of carbon (C), germanium (Ge), and tin (Sn) using an 0.8 Å probe. The Si crystal model with $a = 5.42$ Å was used, but all

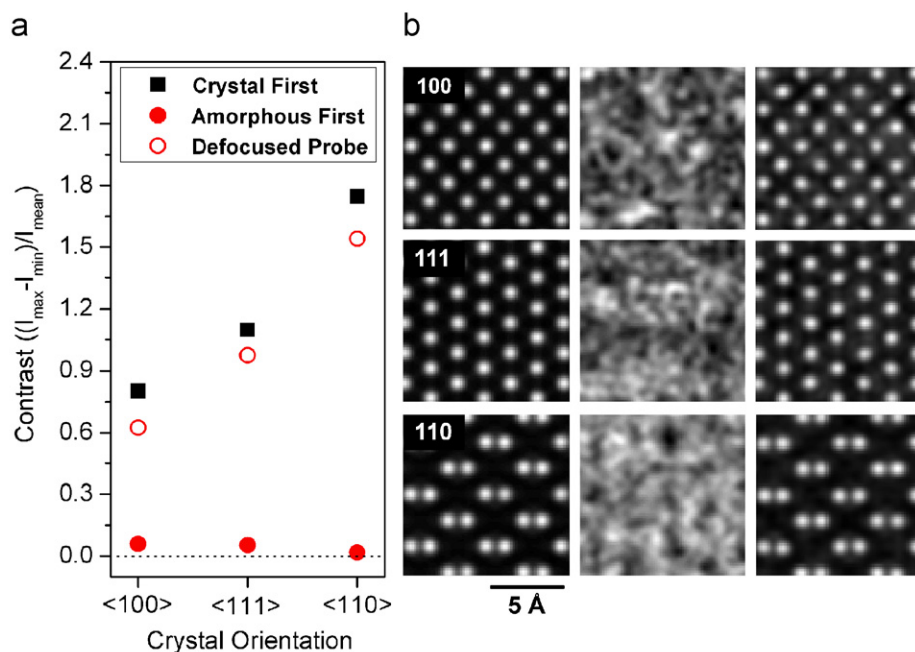

Fig. 7. (a) Calculated contrast in ADF-STEM images of atomic columns in Si specimens with 50% amorphous and 50% crystalline layers for three major crystallographic orientations using a 0.8 Å probe. (b) The actual calculated ADF images: Left panel—beam propagates through the crystal first. Middle panel—beam propagates through the amorphous layer first. Right panel—the same samples as middle panel but now beam is focused (or "defocused" from surface) on the entrance surface of the crystalline portion. Orientations of the crystalline layers are indicated in top left corners. All images are individually scaled to fill available grayscale.

atoms of Si were replaced with atoms of C, Ge and Sn, respectively. In all calculations the probe was focused on and propagated through the amorphous layer first and then through the crystal since this is the case when imaging the columns appears to be the most challenging. Reference linescans from ADF images of pure crystals of silicon (300 Å thick) and the three hypothetical samples are shown in Fig. 8(a). As can be seen I_{min} and I_{max} increase with increasing atomic number with the exception of I_{max} for Sn. The contrast, however, changes in the opposite direction—it decreases with increasing atomic number with C being an exception (see Fig. 8(b)).

The variations of contrast for atomic columns when calculated with different proportions of crystalline and amorphous layers are presented in Fig. 8(b). Here simulations indicate three critical results: (i) the contrast starts to appear (and the column becomes visible) only when the thickness of the amorphous layer is less than 30% of the total thickness independent of the type of the atoms, (ii) starting from Si the contrast of the columns becomes weaker with increasing Z of the atoms and finally, (iii) comparing carbon atoms to Si, not only does the entire ADF intensity drop dramatically, but also the contrast.

3.2.3. *Different specimen thickness*

The visibility of the atomic columns in ADF images as a function of the thickness of the specimen is studied by calculating ADF images for Si specimens using the 0.8 Å electron probe. Here, specimens with 50% amorphous and 50% crystalline layers were considered. The electron beam was oriented along the [1 1 0] crystallographic direction. Specimens were chosen to have a thickness ranging from 50 to 500 Å. Simulated images for five different thicknesses are presented in Fig. 9.

When the electron beam propagates through the crystal first, the visibility of the columns is strong and almost unaffected by an increase in thickness (see Fig. 9(a) top row), whereas in cases when the beam is focused on and propagates through the amorphous layer first the changes are quite significant. Here the columns are visible when the specimen is only 50 Å but become completely unresolvable when the thickness is over 150 Å (see Fig. 9(a) middle row). However, the visibility of the atomic columns is restored when the incident beam is focused not at the sample entry surface but defocused to a depth inside the specimen where the crystalline portion starts (see Fig. 9(a) bottom row). For quantitative analysis the dependence of the contrast on the thickness of the specimen calculated using Eq.(2) is presented in Fig. 9(b).

The contrast of the columns, as calculated when the probe propagates through the crystal first, shows a reduction in contrast, going from $\xi = 3.2$ for 50 Å specimen to $\xi = 1.80$ for 500 Å. When the beam is focused on the specimen entry surface and propagates through the amorphous layer first, the contrast practically disappears for specimens with thicknesses greater than 150 Å. In this case, if the beam is focused where crystalline portion starts, contrast is recovered but it is still lower than when beam enters the crystal first.

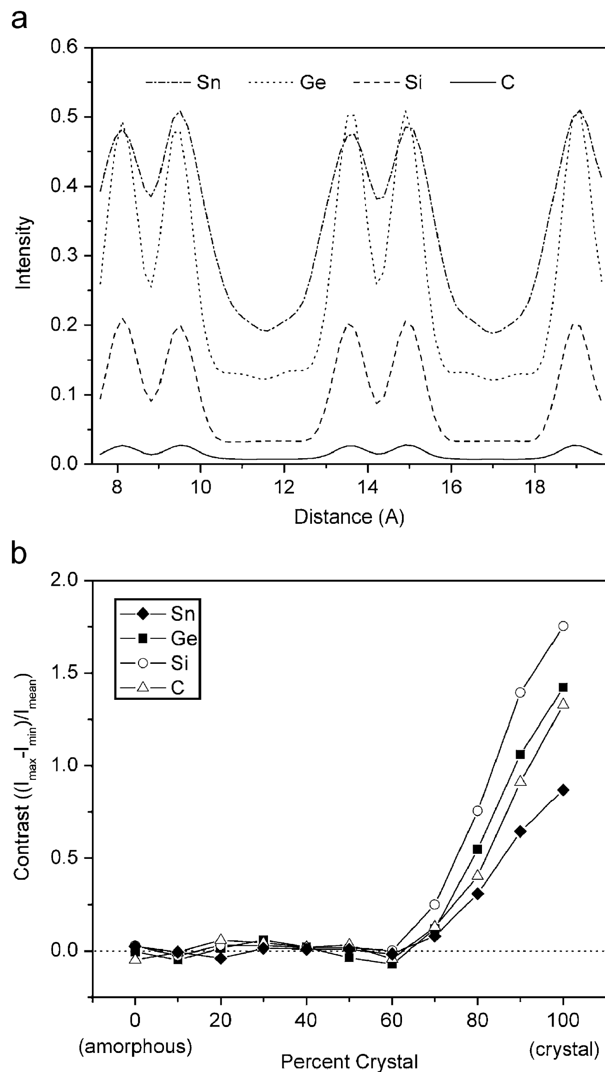

Fig. 8. (a) Linescans from ADF images calculated for Si and for three hypothetical crystals constructed by using the lattice structure of Si and lattice sites occupied with C, Ge or Sn. In all cases the linescans are taken across the dumbbells. (b) Calculated contrast for the four 300 Å specimens when the beam propagates through the amorphous layer first.

4. Discussion

The results presented in the previous section can be summarized as follows: (i) the contrast (visibility) of the atomic columns in ADF-STEM images is always greater when the beam propagates through a crystalline layer first (this holds for both corrected and uncorrected probes); (ii) for specimens with an amorphous layer at the probe entry surface ADF images lose contrast with increasing thickness more quickly with a corrected (0.8 Å) probe than with a uncorrected (2 Å) probe; (iii) the contrast of the atomic columns in crystalline or partially crystalline specimen is highly sensitive to the crystal structure and the types of the atoms present in the crystal; and, finally, (iv) the contrast is also strongly dependent on the total specimen thickness.

Before discussing these results in detail the ambiguities arising from the choice of contrast definition should be addressed. Three different definitions of contrast can be considered. The analysis presented in Appendix A shows that the actual values for the contrast vary from one definition to the next. However, the behavior of the contrast as a function of the amount of amorphous and crystalline layer present in the specimens, or relative contrast, is qualitatively the same.

To understand the poor visibility of the atomic columns in ADF-STEM images due to specimens with an amorphous layer at the surfaces it is essential first to study changes in the incident probe during its propagation through an amorphous layer.

4.1. Beam propagation in a-Ge

The effects of the amorphous layer on the STEM probe were studied. The calculations were performed on a-Ge samples where a relatively high Z-number ensures strong scattering of the incident beam electrons from the specimen. The parameters of the simulations were kept the same as in the previous simulations carried out for silicon (see Section 2). First an aberration-corrected probe of 0.8 Å for a 100 kV STEM was generated (see Fig. 1). This probe was then propagated through a-Ge of different thicknesses. The distribution of the electrons exiting the specimens was obtained in each case in real and reciprocal space. The distribution in real space shows the actual shape of the beam after passing through the amorphous layer. The distribution in reciprocal space (the CBED pattern) describes the angular spread. Simple ray diagrams showing differences between beam propagation through the amorphous layer and through empty space are presented in Fig. 10.

Fig. 11(a) shows the shape of the probe after propagating through 150 Å of a-Ge, wherein strong broadening of the probe is apparent. The corresponding changes in the distribution of probe electrons in reciprocal space are presented in Fig. 11(b). When the beam passes through the amorphous material, part of the incident probe electrons do not scatter at all and after leaving the material behave in exactly the same way as the probe electrons that have "additional" defocus equal to the thickness of the specimen (see Fig. 10). To demonstrate this, a probe with a defocus corresponding to 150 Å of amorphous material, $\Delta f_{\rm new} = \Delta f_{\rm old} - 150\,\text{Å} = -180\,\text{Å}$, was also calculated and the resulting intensity distribution is presented in Fig. 11(c). Similarities between Figs. 11(a) and (c) are apparent. To estimate the contributions of the unscattered and scattered electrons in the probe after passing through a thickness t of amorphous material, the real and reciprocal space distributions of the probe were examined.

As can be seen from Fig. 11(b) (see insert) some of the probe electrons during propagation through the a-Ge scatter into large angles and, therefore, cannot be part of the unaltered probe that has traveled a distance t. Some electrons scatter but still stay in the 0–25 mrad angular range of the incident probe. These scattered electrons

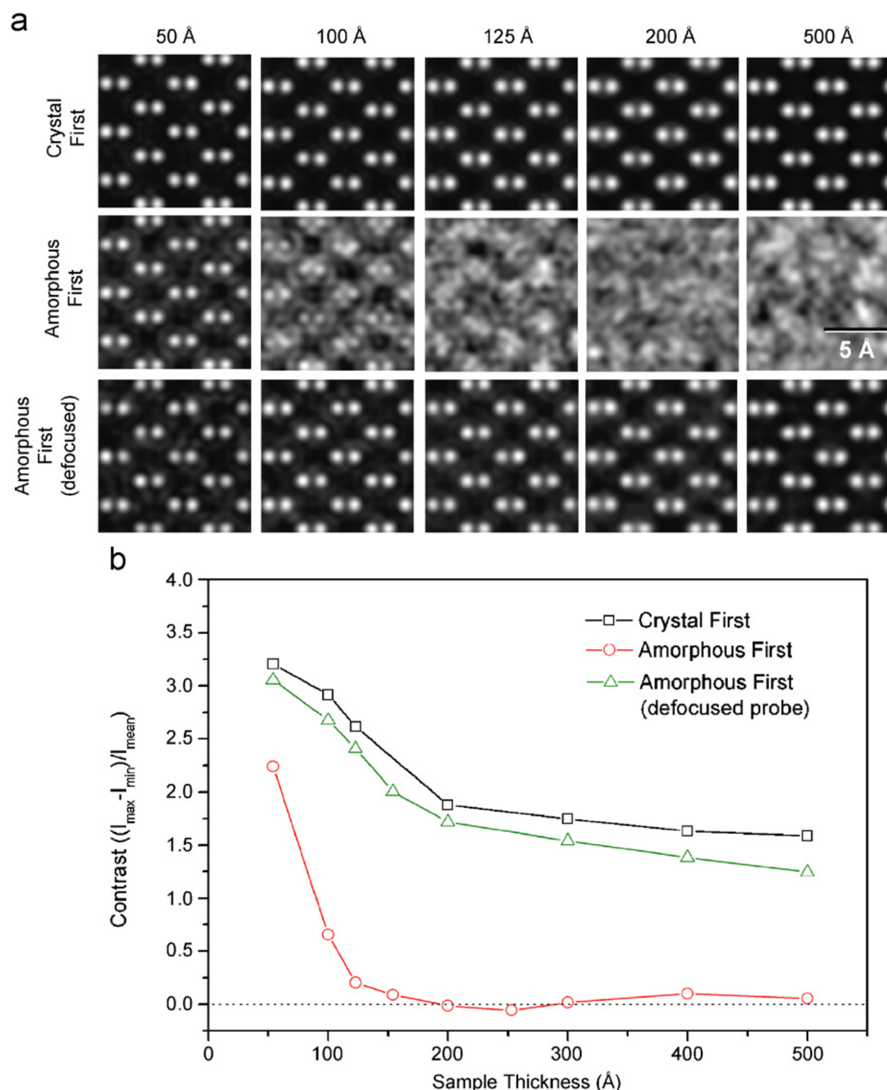

Fig. 9. (a) Simulated ADF-STEM images of silicon specimens consisting of 50% amorphous and 50% crystalline layers calculated with 0.8 Å probe. Crystals were oriented along the [1 1 0] crystallographic direction. Images in top row were calculated for 50, 100, 150, 200 and 500 Å thick specimens when the probe is propagating through the crystalline layer first. Images in the middle row were calculated when the probe is propagating through the amorphous layer first, and the images in bottom row were calculated from the same samples as in middle row correspondingly but now the beam is focused (or ''defocused'' from surface) at the entrance surface of the crystalline portion. All images are individually scaled to fill available grayscale. (b) Calculated contrast of the atomic columns corresponding to the images in (a).

cannot be distinguished from electrons in the original probe and, therefore, they should be considered as part of the unscattered probe.

The number of probe electrons scattered to high angles was calculated by integrating the azimuthally averaged distribution of the intensities in reciprocal space from 0 to 25 mrads before and after the beam is propagated through 150 Å of a-Ge and subtracting one from other (see shaded region in Fig. 11(b) (inset)). Now removing this amount from a new simulated probe with extra defocus, $\Delta f_{\text{new}} = -180$ Å, the two results were compared in Fig. 11(d). The difference between the probe propagated through a-Ge and the new, extra defocused probe (reduced) is a Gaussian-like background. The existence of a Gaussian-like background in the probe, after propagating through an amorphous layer, has been reported previously in the example of InP [11].

The effect of this Gaussian-like background is best visualized when the probe is propagated through 150 Å of a-Ge and is then fit with a sum of the Gaussian background and the new defocused probe with appropriately reduced intensity. This is presented in Fig. 12(a). Analysis conducted for the probes propagating through different thicknesses of a-Ge shows a similar result. However, with an increase in the thickness of the amorphous Ge layer the Gaussian background becomes broader. These backgrounds calculated for a probe after 77, 150 and 300 Å of a-Ge are presented in Fig. 12(b). Despite broadening of the peak, the intensity under the Gaussian background is higher when thicker amorphous layers are considered. The

analysis of these Gaussian backgrounds aimed to study beam broadening inside amorphous materials due to scattering (see inset in Fig. 12(b)) shows that their FWHM closely follows an empirical $t^{3/2}$ thickness dependence suggested by Goldstein et al. [24].

The effect of the beam propagation through an amorphous layer of thickness t can be considered as a sum of the partial original probe that has now traveled an extra distance, t, and a Gaussian background centered at the position of the incident probe.

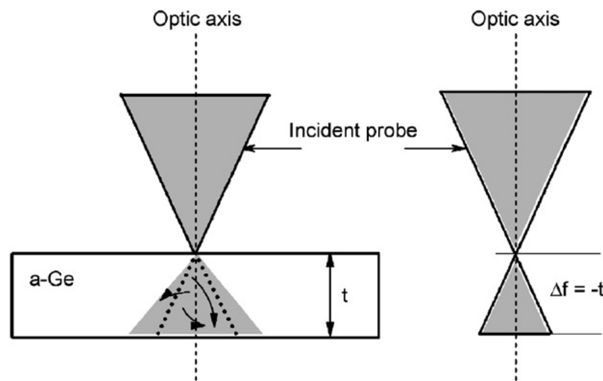

Fig. 10. A ray diagram of the aberration-corrected probe that propagates through a layer of a-Ge of thickness t (left), and the same probe that travels the same distance t through empty space (right).

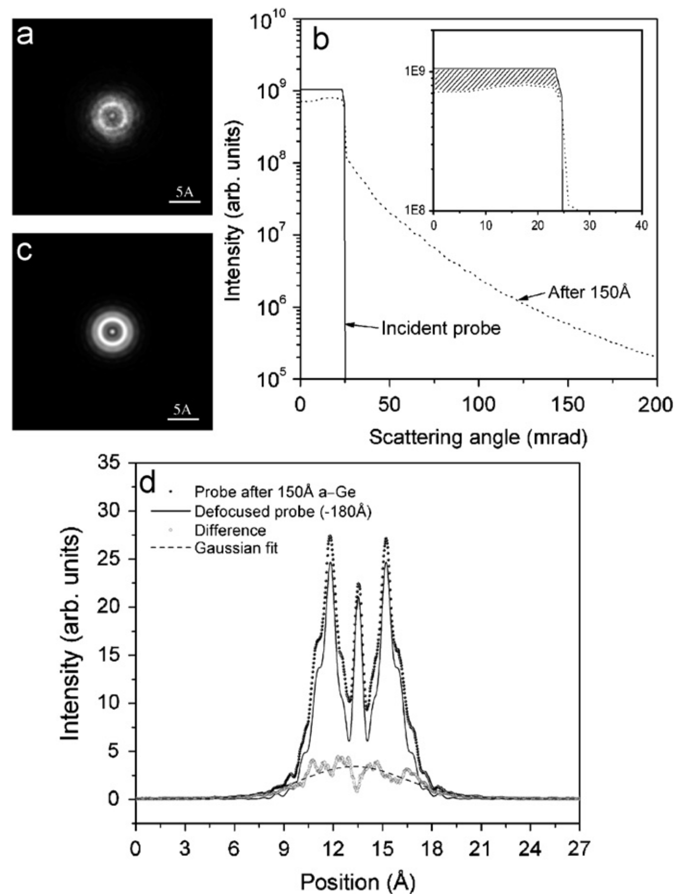

Fig. 11. (a) Intensity distribution of 0.8 Å incident probe after passing through 150 Å of a-Ge. (b) Intensity distribution of the same probe in reciprocal space (azimuthally averaged) together with incident probe. Inset is a close-up of the 0–40 mrad region. (c) New probe calculated using initial probe with additional defocus of $\Delta f = -150$ Å. (d) Linescan of the intensities from (a) and (c) with appropriate reduction and the difference between these two fit with a Gaussian function.

4.2. Effect of amorphous layer on imaging

The results presented in the previous section show that after the beam propagates through an amorphous material some of the initial intensity transforms into a Gaussian-like background and the remaining intensity experiences an additional change of defocus corresponding to a distance t equal to the thickness of the amorphous material. This suggests that the primary reason for the low visibility of the atomic columns with an amorphous layer at the entry surface is the loss of the spatial resolution due to significant beam traveling. This effect is independent of material in the amorphous layer. Probes with different defocus values corresponding to a beam traveling through different thicknesses of amorphous layers are presented in Fig. 13. As can be seen, the probe shape degrades dramatically even with changes in Δf value as small as 60 Å. The changes in the ADF transfer function corresponding to such variation in defocus are presented in Fig. 1(b). These results are consistent with observations by Borisevich et al. [25] suggesting a possibility for depth sectioning of amorphous specimens by obtaining through-focal series ADF images using an aberration-corrected STEM.

Calculations of the uncorrected probe with similar changes in defocus (not presented here) show that the shape of the probe changes only very slightly. The depth of focus for the 2 Å probe is about 180 Å. This weak sensitivity of the uncorrected STEM probe to defocus value (visible changes in the probe shape occur only when Δf is changed by $\gtrsim 250$ Å) explains why, in cases when a 2 Å probe is used, changes in the visibility of atomic columns in ADF images are small (see Fig. 3).

The amounts of the initial probe intensity transformed to a Gaussian background are different for different amorphous materials with the same thickness. Heavier atoms in the amorphous layer create stronger background. However, since the primary alteration of the probe resolution is due to the extra distance traveled (i.e., thickness of the amorphous layer), it is not surprising that complete loss of visibility in C, Si, Ge and Sn samples occurs when the specimens have exactly the same thickness of the amorphous layer, $t = 120$ Å, at the beam entry surface (see Fig. 8(b)).

4.3. Improving visibility in ADF images in presence of amorphous layer

The results of the previous sections also provide a solution for improving the visibility of the atomic columns

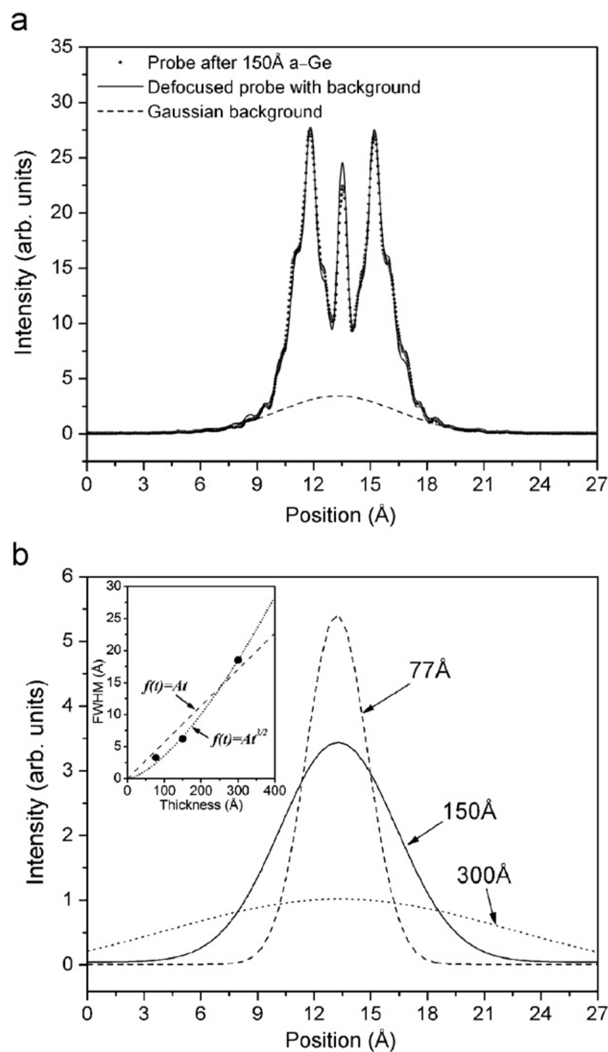

Fig. 12. (a) Linescan of the probe after passing through 150 Å of a-Ge fit with the sum of Gaussian background and unscattered probe (reduced probe with extra Δf). The corresponding Gaussian background is also plotted. (b) Gaussian backgrounds obtained from a probe propagated through 77, 150 and 300 Å a-Ge. The inset shows that FWHM of these Gaussian backgrounds closely follows $t^{3/2}$ thickness dependence.

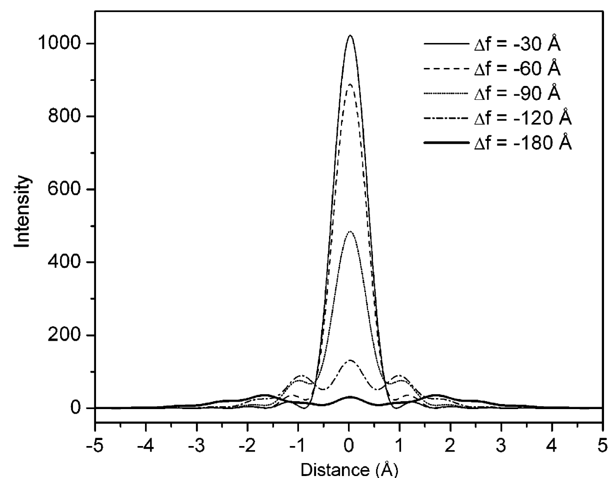

Fig. 13. Line profiles of the STEM probes. These probes are normalized to the same total intensity. The optical parameters used in the calculations were: $E_0 = 100\,\text{kV}$, $C_{s(3)} = -0.015\,\text{mm}$, $C_5 = 10\,\text{mm}$, $\alpha_{obj} = 25\,\text{mrad}$, and defocus values are as indicated.

in high-resolution ADF-STEM images. For thin layers of amorphous material only a small portion of the incident beam scatters and becomes background. Therefore, it is possible to defocus the incident probe initially by such an amount that after it propagates through the amorphous layer it will be properly focused at the desired depth (with a small background from beam scattering). For example, if the beam propagates through 50 Å of amorphous material, it is necessary to change the initial defocus value of the probe to $\Delta f_{new} = \Delta f_{old} + 50\,\text{Å}$.

The previous calculations of ADF images of Si consisted of 150 Å amorphous and 150 Å crystalline layers with the 0.8 Å STEM probe, and these showed that the ADF images have contrast of $\xi = 0$ (see Fig. 7). However, when a new incident probe is generated with a defocus value of $\Delta f_{new} = 120\,\text{Å}$, the result is a clear image of the atomic columns. This is illustrated in Fig. 14. To confirm that a

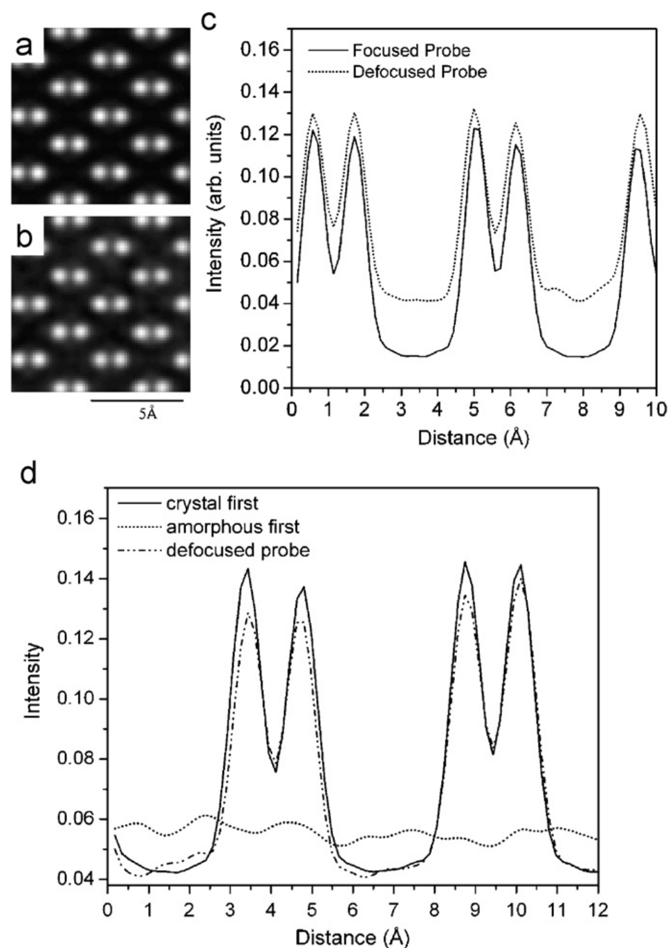

Fig. 14. (a) ADF image of 150 Å of a pure crystalline silicon sample imaged using a 0.8 Å probe. (b) ADF image of the silicon specimen consisting of 150 Å amorphous and 150 Å crystalline layers, and imaged using a probe with defocus of $\Delta f_{new} = 120\,\text{Å}$. The images are individually scaled to fill available grayscale. (c) Linescans from the ADF images in (a) and (b). The contrast of the atomic columns in (a) is $\xi = 3.2$ and in (b) $\xi = 1.5$. (d) Comparison between linescans from ADF images in (b) and one from specimen with 150 Å crystalline and 150 Å amorphous layers.

Gaussian background is also generated during the process of the probe passing through the amorphous layer, the results are compared with a simulated ADF image of 150 Å pure crystalline silicon. As was expected, the contrast of the later image, $\xi = 3.2$, is more than twice that of the first, $\xi = 1.5$.

5. Conclusion

Study of high-resolution ADF imaging in uncorrected and aberration-corrected STEMs by multislice image simulations shows that the presence of an amorphous layer at the surface of the specimen can significantly alter the visibility of the atomic columns. To achieve the best possible contrast in ADF-STEM imaging it is essential to remove the amorphous layers from both surfaces of the specimen. The reduction of the contrast due to the presence of the amorphous layer is strongly dependent on the thickness of the layer. For aberration-corrected 0.8 Å probes approximately linear reduction of the contrast (with a slope of 1) is expected with an increase in the thickness of the amorphous layer. Also an amorphous layer at the beam entry surface clearly effects the image contrast more than the layer at the exit surface when the probe is focused always upon the entry surface of the specimen. The simulations also show dependence of the image contrast on the crystal structure and orientation and the types of atoms present in the crystal.

Detailed analysis indicates that after propagating through the amorphous layer a portion of the beam passes without any alteration while the rest scatters to larger angles creating a Gaussian background. The portion of the beam that passes without scattering loses spatial resolution due to the additional distance traveled by the beam which ultimately broadens the beam. For an aberration-corrected 0.8 Å probe, traveling through 60 Å of amorphous material or even empty space is sufficient to lose resolution. After passing through 120 Å of amorphous material the beam transforms so dramatically that no atomic columns can be resolved in the crystal layer below. Due to the fact that the 2 Å non-corrected probe is not very sensitive to the defocus value, the presence of the thin ($\lesssim$200 Å) layer of amorphous material should not significantly affect the visibility of the atomic columns. However, low contrast should be expected.

These results also suggest that with appropriate changes in defocus value specimens with amorphous layers on the top (beam entry surface) can also be imaged and high-resolution ADF images with substantial contrast of atomic columns can be obtained. However, compared with a clean (amorphous free) specimen an additional increase of the background should be expected.

Acknowledgments

This work is supported by the Nanoscale Science and Engineering Initiative of the NSF EEC-0117770 and NYSTAR C-020071.

Appendix A

A.1. Contrast in ADF-STEM images

The definition of the contrast (or visibility) of atomic columns in images (including ADF-STEM images) has some ambiguity. It can be defined in three different ways:

$$\xi_1 = \frac{I_{\max} - I_{\min}}{I_{\min}}, \quad (3)$$

$$\xi_2 = \frac{I_{\max} - I_{\min}}{I_{\text{mean}}}, \quad (4)$$

$$\xi_3 = \frac{I_{\max} - I_{\min}}{(I_{\max} + I_{\min})/2}. \quad (5)$$

Here $I_{\max}$ is the intensity of the image at the position of the atomic column, $I_{\min}$ is the intensity in between the columns and I_{mean} is the mean intensity of the entire image. All three definitions represent the visibility of the features, in this case the atomic columns, relative to the background. The difference, however, is in the description of the background. Depending upon which definition is used, a different actual value of the contrast can be obtained from the same image.

To show the differences in the actual values of the contrast for the three definitions (3)–(5), the contrast of the atomic columns in ADF-STEM images was calculated from simulated images generated using an aberration-corrected probe (see Fig. 5). The results are presented in Fig. 15. As was expected, the values for the contrast are different: the highest when the minimum values in the images were considered as a background (3). The difference between contrasts ξ_2 and ξ_3, however, depend on the two-dimensional density of the atoms in the imaging plane and on the STEM probe size: as the probe size increases and

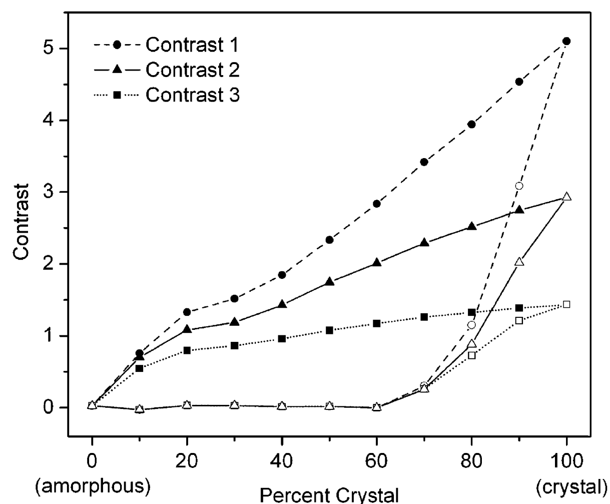

Fig. 15. Contrast variation of the atomic columns in ADF-STEM images calculated for 300 Å thick silicon specimens with a 0.8 Å probe using three different definitions of the contrast. The contrast is shown as a function of percentage of amorphous layers for two cases—the beam propagates through the crystal first and through the amorphous layer first. For comparison see Fig. 6. The crystalline portion is in the [1 1 0] orientation.

atomic columns become closer the values of ξ_2 and ξ_3 approach each other.

As can be seen from Fig. 15, all three definitions show similar behavior: the contrast is significantly higher in ADF images when the beam propagates through the crystalline layer first than when the amorphous layer is first. Calculations performed with a 2 Å STEM probe (not presented here) also show similar results. It appears that for understanding changes in the visibility of the atoms in the ADF-STEM images it is not critical which definition is used.

References

[1] J.P. Benedict, R. Anderson, S.J. Klepeis, M. Chaker, Mater. Res. Soc. Symp. Proc. 199 (1990) 189.
[2] J.P. Benedict, R. Anderson, S.J. Klepeis, in: R. Anderson, B. Tracy, J. Bravman (Eds.), Specimen Preparation for Transmission Electron Microscopy of Materials—II, Materials Research Society, vol. 254, Boston, MA, 1992, p. 121.
[3] S.J. Klepeis, J.P. Benedict, R.M. Anderson, in: J.C. Bravman (Ed.), Specimen Preparation for Transmission Electron Microscopy of Materials, Materials Research Society, vol. 115, Pittsburgh, PA, 1988, p. 179.
[4] P.J. Goodhew, Thin Film Preparation for Electron Microscopy, in: Practical Methods in Electron Microscopy, vol. 11, Elsevier, Amsterdam, 1985.
[5] A. Barna, Mater. Res. Soc. Symp. Proc. 254 (1992) 3.
[6] K.A. Mkhoyan, J. Silcox, Appl. Phys. Lett. 82 (2003) 859.
[7] D.A. Muller, J. Silcox, Philos. Mag. A 71 (1995) 1375.
[8] P.E. Batson, O.L. Krivanek, N. Dellby, Nature 418 (2002) 617.
[9] P.D. Nellist, M.F. Chisholm, N. Dellby, O.L. Krivanek, M.F. Murffit, Z.S. Szilagyi, A.R. Lupini, A. Borisevich, W.H. Sides, S.J. Pennycook, Science 305 (2004) 1741.
[10] K.A. Mkhoyan, P.E. Batson, J. Cha, W.J. Schaff, J. Silcox, Science 312 (2006) 1354.
[11] S. Hillyard, Ph.D. Thesis, Cornell University, Ithaca, NY, 1995.
[12] T. Yamazaki, K. Watanabe, N. Nakanishi, I. Hashimoto, Ultramicroscopy 99 (2004) 125.
[13] J.M. Cowley, A.F. Moodie, Acta Crystallogr. 10 (1957) 609.
[14] R.F. Loane, P. Xu, J. Silcox, Acta Crystallogr. A 47 (1991) 267.
[15] J. Silcox, P. Xu, R.F. Loane, Ultramicroscopy 47 (1992) 173.
[16] S. Hillyard, R.F. Loane, J. Silcox, Ultramicroscopy 49 (1993) 14.
[17] D.O. Klenov, S. Stemmer, Ultramicroscopy 106 (2006) 889.
[18] R.F. Loane, E.J. Kirkland, J. Silcox, Acta Crystallogr. A 44 (1988) 912.
[19] D.A. Muller, B. Edward, E.J. Kirkland, J. Silcox, Ultramicroscopy 86 (2001) 371.
[20] K.A. Mkhoyan, E.J. Kirkland, J. Silcox, E.S. Alldredge, J. Appl. Phys. 96 (2004) 738.
[21] E.J. Kirkland, Advanced Computing in Electron Microscopy, Plenum Press, New York, 1998.
[22] P.E. Batson, Ultramicroscopy 106 (2006) 1104.
[23] S. Hillyard, J. Silcox, Mater. Res. Soc. Symp. Proc. 332 (1994) 361.
[24] J.I. Goldstein, J.L. Costley, C.W. Lorimer, in: O. Jahari (Ed.), Scanning Electron Microscopy, 1977, p. 315.
[25] A.Y. Borisevich, A.R. Lupini, S.J. Pennycook, Proc. Natl. Acad. Sci. 103 (2006) 3044.